ROYAL AERONAUTICAL SOCIETY

REGULAR PAPER

Experimental evaluation of the drag curves of small fixed wing UAVs

A. Weishäupl [iD], L. McLay [iD] and A. Sóbester

Aeronautics and Astronautics, University of Southampton, Southampton, UK
Corresponding author: A. Weishäupl; Email: aw6g15@soton.ac.uk

Abstract

Tight budgets often limit the scope of test campaigns within the development programmes of small uncrewed air vehicles (UAVs). This paper explores a range of combinations of instrumentation suites and protocols for both wind tunnel and flight evaluation, focusing on the key aspect of drawing up the drag curve of the airframe. Through extensive testing of a 5kg maximum take-off mass, fixed wing, twin motor, richly instrumented test platform, we show that automated glides over a range of airspeeds and the slow down manoeuvre are effective ways of determining power-off drag, while estimating thrust from propeller speed, and voltage and current sensing based methods work well for the power-on case. We also seek the most time-efficient and robust mix of the above manoeuvres to yield a given drag curve accuracy level and we find wind condition impacts the manoeuvre makeup of the optimal strategy.

Nomenclature

a	acceleration (m/s^2)
$\mathit{\!R}$	aspect ratio (-)
b	wing span (m)
c	mean aerodynamic chord (m)
C_D	drag coefficient (-)
C_{D0}	zero lift drag coefficient (-)
C_L	lift coefficient (-)
C_{L0}	zero angle-of-attack lift coefficient (-)
$C_{L\alpha}$	lift curve slope (1/deg)
C	capacity (Ah)
D	drag (N)
e	Oswald span efficiency (-)
E	endurance (s)
h	height (m)
I	current (A)
K	lift induced drag constant (-)
L	lift (N)
m	mass (kg)
n	Peukert coefficient (-)
P	power (W)
Q	charge (C)
Rt	battery hour rating (-)
S	wing area (m^2)
SOC	state of charge (-)
t	time (s)
T	thrust (N)

U	voltage (V)
U_{ave}	average voltage (V)
V_{D}	dive airspeed (-)
V_{IA}	indicated airspeed (m/s)
V_{NE}	never exceed airspeed (m/s)
V_{S}	stall airspeed (m/s)
V_{TA}	true airspeed (m/s)
w_1, w_2	objective function weights (-)
W	weight (N)

Greek symbols

α	angle-of-attack (deg)
γ	climb angle (deg)
η_{col}	Coulombic efficiency (-)
η_{tot}	total efficiency (-)
θ	pitch (deg)
$\hat{\mu}_{\mathrm{e}}$	normalised mean error (-)
ρ	density (kg/m³)
σ	standard deviation (-)
$\hat{\sigma}$	normalised standard deviation (-)
Ω	rotation speed (rad/s)

Subscripts

i	index
MAX	maximum
x, y, z	axis system

1.0 Introduction

Fitting (UAVs with on-board sensors and performing flight tests is a convenient way to collect extensive performance data about the platform. In this paper we focus on the lift and drag curves at low mach numbers, as they are the starting point of most performance calculations, operational simulations and contingency analyses. There is a rich literature around the estimation of drag curves on small, uncrewed, fixed wing platforms, ranging from methods based on battery energy depletion [1], to thrust estimation [2–6] and to methods involving unpowered manoeuvres [7–11]. We are, however, not aware of any systematic comparisons of these methods, in terms of their accuracy and ease of implementation, and filling this gap is the goal of this paper. The best choice of method depends on several factors, including the desired accuracy, required equipment cost and mass and any platform-specific limitations (for example whether the propulsion system can be safely stopped and restarted at will). In this paper, we compare several different methods on a medium-size low-cost off-the-shelf UAV. We discuss the use of additional sensors to aid in determining the coefficients of lift and drag, and the advantages and disadvantages of various methods. We reference the numerical results against full scale wind tunnel data (in fact, our choice of test platform size was driven by the desire to be able to conduct wind tunnel tests without significant blockage effects). Finally, we explore a manoeuvre strategy optimisation for determining the most accurate combination of two such manoeuvres given a flight test time limit.

Before we delve into the details of experimental lift and drag estimation for small UAVs, let us consider the circumstances in which the effort invested in doing this is warranted, or even unavoidable. An electric consumer drone designed for a very simple mission, with a fixed and constant payload, can probably be brought to market without a profound understanding of its lift and drag curves; after all, its range and endurance could be established simply by flying the vehicle to battery exhaustion in a range of conditions, which would place a pair of practically sufficiently accurate bounds on those numbers. However, complex and flexible missions, variable (potentially externally slung) payloads and/or a

Figure 1. *SPOTTER environmental monitoring drone releasing its payload.*

requirement for optimal mission planning can bring the need for an intimate understanding of the drag curves in sharp relief.

Consider the example of the drone pictured in Fig. 1 (the SPOTTER long-endurance environmental-monitoring platform). Powered by a 'mild hybrid' propulsion system, it can carry (and, if needed, release) a 5kg payload of arbitrary shape and size (limited, of course, by the size of the aircraft itself). In the mission illustrated in Fig. 1 this payload is a miniature, robotic submarine, which SPOTTER delivers to its target, then, following the release and splashdown of the underwater vehicle, it loiters in the area to serve as a communications relay, before returning to base with a target contingency fuel reserve in its tank on arrival.

The mission planning, in this case, is a complex, constrained optimisation problem, the objective function computation for which needs to account for the drag of the platform with and without the submarine attached, with and without flaps deployed, and at a range of speeds and weights. The search needs to visit a large number of different mission scenarios with different times spent in the various configurations, at different speeds and at an ever-changing weight. The pressing need for exact lift and drag curves evident in this case does not end here either – in case of contingencies (for example, if the wind changes partway through the mission, the payload fails to release, the flaps fail to retract/deploy, etc.), the on-board intelligence of the autopilot must be able to re-plan its tasking accordingly (ideally with error margins attached, obtained, for example, through an ensemble of Monte Carlo runs of the performance model). Once again, attempting to do this with with rudimentary baseline performance guesses carries vast penalties in terms of unnecessarily conservative fuel reserves (such as McCrink and Gregory [7] who took off with $\sim 190\%$ more fuel than the mass calculated to complete the mission), unnecessarily aborted missions, or, worse, accidents caused by fuel starvation.

In the case of more sophisticated platforms, flight management systems capable of working towards a specified cost index (the ratio of time related cost of aircraft operation to fuel cost), also need a reliable set of aerodynamic coefficient values.

Finally, a caveat. Some of the techniques described in this paper assume that the propulsion system of the aircraft can be fully shut down and restarted at will, safely, and multiple times. Caution is advised with wet fuel based systems that have a specific re-light envelope (in terms of speed, temperature, and density altitude) – taking such limitations into account is beyond the scope of this work.

2.0 'FliTePlat'

'FliTePlat' (Flight Test Platform – Fig. 2, [flɪteplæt]), the aircraft we built to perform the test campaign reported in this paper, is based on a low-cost, off-the-shelf airframe [12]. This is of a foam construction

Table 1. *FliTePlat key parameters.*

Variables	Values
Geometry	
Wing span, b	1.96m
Reference area, S	0.488m^2
Mean aerodynamic chord, c	0.275m
Length	1.07m
Fuselage height	0.18m
Propeller diameter	304.8mm (12")
Propeller pitch	152.4mm (6")
Number of blades	2
Performance	
Maximum allowable take-off mass, m	5.5kg
Manufacturer recommended cruise indicated airspeed	20m/s
1g stall airspeed	11m/s
Maximum dive airspeed	37m/s

Figure 2. *FliTePlat – Flight Test Platform – during a low pass.*

with composite spars; see Table 1 for its key parameters. Its simple and rugged flight control layout consists of a pair of ailerons and a pair of ruddervators mounted on a V-tail. In the spirit of simplicity and cost minimisation it does not have a conventional undercarriage; instead it is hand-launched or deployed via a take-off trolley (Fig. 3) and recovered through belly-landing. Its flight envelope is limited at minimum and maximum load factors of around 0.2 to 3.8 for respectively, the latter mostly due to wing deformation causing loss of lift. This design philosophy is yet another attractive feature from an aerodynamic flight testing point of view, as exceeding the limits of the flight envelope is unlikely to cause structural failure and thus loss of relatively expensive (by small drone standards!) test instrumentation (except, potentially, when exceeding V_{NE}, which is set by flutter constraints, to around 37m/s for FliTePlat).

The system identification task at the core of this paper requires a diverse instrumentation and control suite, which we implemented on board FliTePlat around the following key components (see Fig. 4 for a visual representation):
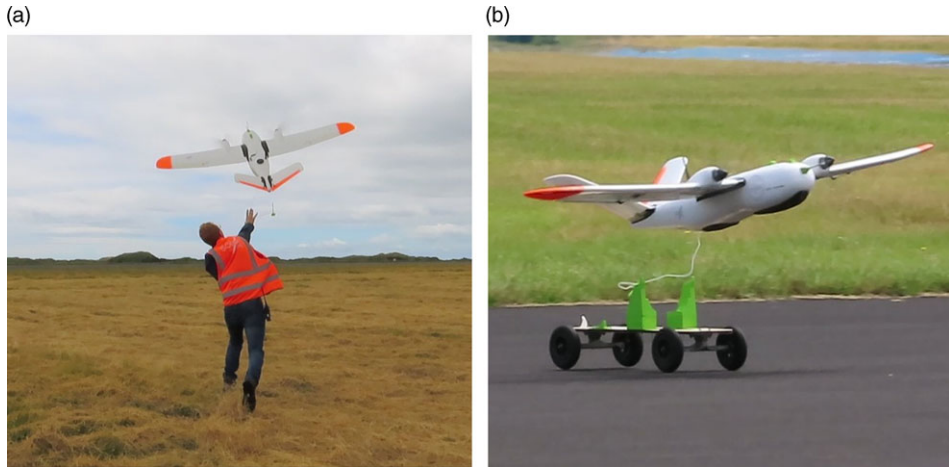
Figure 3. *Two launch methods for FliTePlat: (a) hand launching, (b) trolley launching.*
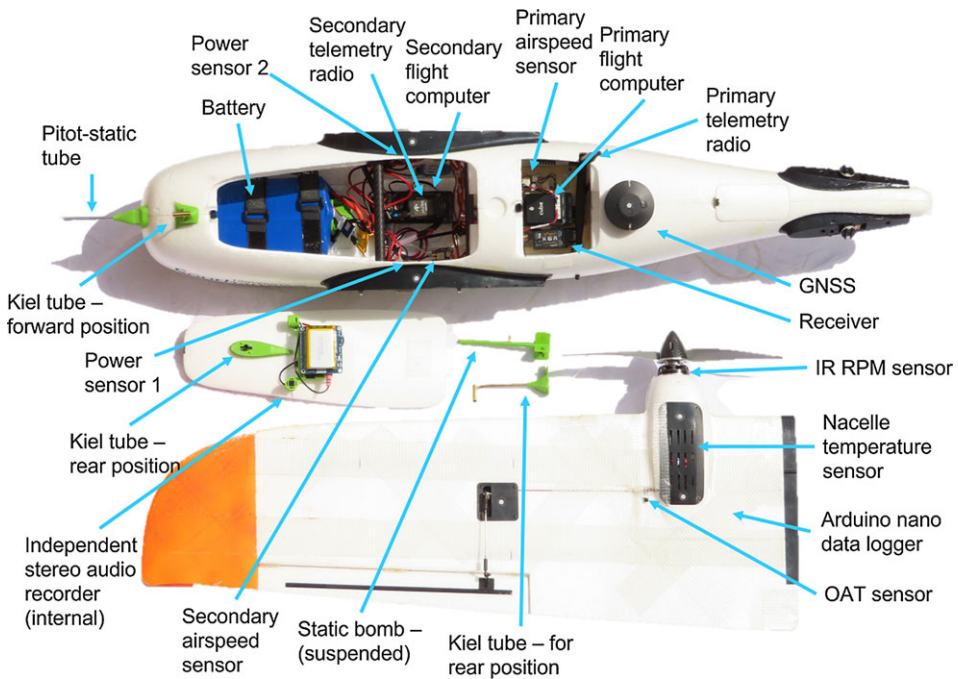

Figure 4. *FliTePlat internal component layout.*

- two separate air data systems (a conventional Pitot-static tube and a Kiel tube and static bomb set up)
- two *PixHawk 2.1 Cube Black* autopilot systems (a primary flight computer and data recorder and an independent secondary data recorder for the second air data system)
- a *Here 2* Global Navigation Satellite System (GNSS)
- two telemetry modules (one for the primary and secondary flight computers respectively)
- voltage and current sensors (power sensor 1 and 2 in Fig. 4) on the power circuits of each motor

- an infrared motor RPM sensing and logging system
- a stereo audio logging capable of record high quality audio data (the audio serves as an additional dimension to the recorded data, for example as an additional means of validating the timestamps of key audible events)
- outside air temperature and nacelle temperature logging

There is no dedicated angle-of-attack sensor on board, a synthetic angle-of-attack is computed as the difference between the pitch and the climb angle. The latter is calculated from the rate of change of the GNSS altitude and the true airspeed. The accuracy of the synthetic angle-of-attack (with respect to the true angle-of-attack) depends on the exact error margins of the GNSS altitude, as well as the differential pressure sensor used to obtain the indicated airspeed employed on the aircraft (as well as the barometric pressure and outside air temperature sensors). Our comparisons with wind tunnel observations indicate good agreement, though the exact margins of the particular sensor suite selected are expected to have a minimal impact on the main goal of the work reported here, which is to compare various methods that use identical sensors.

FliTePlat serves as a test platform for several other experiments, data for which can often be recorded on the flights performed for this paper. This includes the secondary air data system (Kiel tube and static bomb) as well as the secondary *PixHawk 2.1 Cube Black* and telemetry module. This system serves to compare the air data quality between the conventional Pitot-static tube and the angle-of-attack insensitive Kiel tube and static bomb system. There are two mounting positions for the Kiel tube as the effect of these were compared in wind tunnel tests. As these components were present for several of the flights, they have been kept on FliTePlat for a consistent drag with the Kiel tube in the forwards location for all tests. A conventional Pitot-static tube has been chosen over a high fidelity air data boom due to the increased availability and reduced costs involved.

FliTePlat's two wing-mounted electric motors drive two-bladed, fixed-pitch tractor propellers. During unpowered gliding flight, the propellers are electrically locked in place to stop any windmilling; however, the orientation that the propellers come to rest in cannot be chosen. This was preferred over windmilling propellers due to the overall drag reduction, however, does add an element of noise to the data [13]. FliTePlat's electric motors are ideal for repeated segments of unpowered flight due to their rapid restart capabilities, which internal combustion engines of the small UAV scale do not have.

In the next section we discuss in detail the two classes of parameter identification techniques at the centre of this paper: wind tunnel testing and flight testing.

3.0 Methodologies

In this paper the wind tunnel data serves as a carefully controlled baseline for the flight test data, both in terms of cost and parameter identification. We use it as a fixed comparison to the other methods due to its higher repeatability and ease of data collection.

Propulsor – airframe interactions, most significantly the interactions between the prop-wash or the jet wash, and the lifting surfaces of the airframe – have a significant impact on many aspects of the handling and the performance of the aircraft. These include the lift and drag curves of the airframe, where a number of questions arise, especially pertaining to contingencies. How does the loss of one propulsor (on a twin) affect the overall drag, considering that few UAV props have a feathering capability? Does this vary significantly depending on the angle at which the prop stops? What is the drag increment associated with a windmilling propeller (or two)? More generally, how does the prop-wash change the lift generating capability of the wings? Some of these are difficult questions for flight test crews of conventional aircraft to answer accurately (mostly for safety reasons); conversely, with careful autopilot programming and testing, and with an incremental approach, the UAV test engineer has an advantage here (especially, as hinted already, in the case of aircraft powered by electric motors).
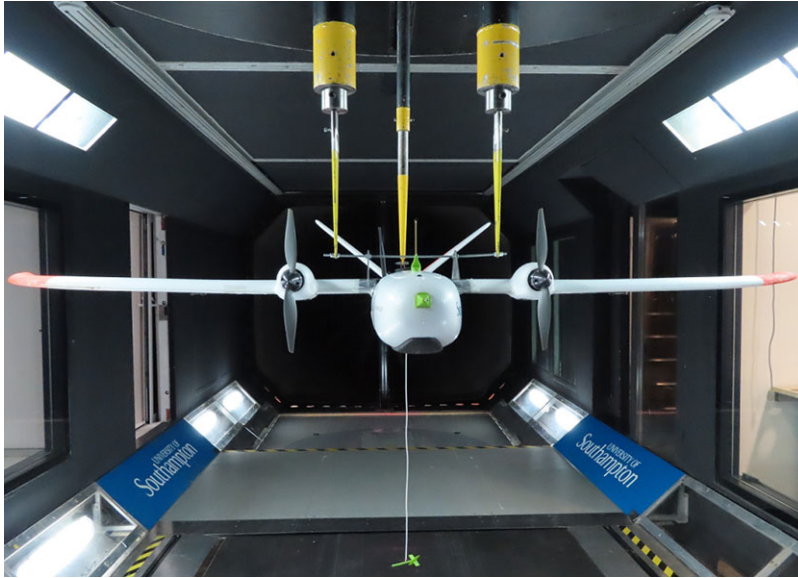
Figure 5. *FliTePlat mounted on the load cell in the R.J. Mitchell wind tunnel.*

To this end, in this paper we consider both power-on and power-off test scenarios, the results of each being important from the point of view of various aspects of the design (e.g. normal operations, full or partial power loss scenarios).

We investigate the following power-on methods: (1) the basic battery depletion method, which measures the charge added to the battery during recharging; (2) the improved battery depletion method, which monitors the voltage and current during the flight and estimates the battery state of charge (SOC) in the post processing; (3) estimating thrust from voltage, current and propeller performance data; (4) estimating thrust from measured propeller rotational speed (RPM); and (5) estimating thrust from audio data.

We consider the following unpowered methods: (1) manual and automated glide slope manoeuvres and (2) the 'slow down' method of drag estimation.

Finally, we briefly discuss other techniques, such as measuring the thrust directly through a load cell, using 3D motion tracking cameras and computational methods.

3.1 Reference – Wind tunnel test

Wind tunnel tests are widely used to obtain approximations of the lift and drag curves. They are especially attractive when their speed range is close to that of the UAV and their test section is large enough to fit the UAV without interference. This makes the data collection process straightforward, and the UAV can be "flown" in a broad range of conditions, including in parts of the flight envelope that are not readily accessible or safe in flight.

We tested FliTePlat in the *R.J.* Mitchell wind tunnel at the University of Southampton. The tunnel has a test section 3.5m wide and 2.4m high, with a windspeed range of 4.0 to 40.0m/s and less than 0.2% turbulence [14]. In our experiments, forces and moments were measured on a six-component overhead balance, with FliTePlat mounted in the centre of the test section (Fig. 5). The tail support was set up to continuously vary the pitch during wind tunnel operation, allowing for accurate positioning of FliTePlat.

Data gathered by the wind tunnel's sensors included the three forces (lift, drag and side force), three moments (pitch, roll and yaw), the yaw and pitch angles, the windspeed and the ambient temperature and

pressure. The wind tunnel's airspeed is calculated from a Pitot-static system located at the beginning of the test section, approximately 40cm from the nearest wall, thus outside of the boundary layer.

As the airflow in the wind tunnel can be assumed to be horizontal, the angle-of-attack can be approximated as the pitch of the UAV. We performed several angle-of-attack sweeps at 14, 16 and 20m/s to recreate the lift and drag curves. At 14m/s, the angle-of-attack could be varied between $-8°$ and $12°$ whereas at 20m/s this was limited to $-4°$ and $4°$ due to reaching the maximum safe load on the lifting surfaces.

Wind tunnels are expensive to maintain and operate [15]. Consider the example of the R. J. Mitchell wind tunnel at the University of Southampton, featuring a 3.6m × 2.5m working section and a maximum windspeed of 40m/s: a day of testing here (around the minimum time needed for accurate drag curve identification) costs £2,850 at the time of writing [14]. This includes a dedicated member of staff and 8h of operating time. The need for a dedicated scale model of the airframe (necessary whenever the size of the working section and the risk of significant wall effects conspire to exclude tests of the actual vehicle in the tunnel) may add further costs and, again, increase the need for skilled personnel [16]. The data collected through a single wind tunnel run may also be subjected to calibration errors [17], resulting in the need to perform repeats on multiple different days, significantly increasing the cost of this already expensive method. Additionally, the clean, clinical conditions created by wind tunnels may offer less by way of real world operational insight in the case of small UAVs.

3.2 Power-on flight testing methods

Power-on methods consist of flight segments where propellers are powered by the flight battery. This includes the basic and improved battery depletion methods, using power sensors to calculate the power for flight and estimating the thrust from airspeed and propeller rotation speed.

In the following methods, the main assumptions are that

- The flight is steady and level with constant airspeed and, hence, zero climb angle and negligible accelerations can be assumed.
- The total efficiency of the powertrain unless stated otherwise is 0.7, based on results by Ref. (1) (this will vary for different powertrain architectures, the true airspeed during the flight segments and how well the components in the powertrain system are matched).

3.2.1 Battery depletion methods

The following methods are based on measuring the power used by the propulsion system throughout a segment of flight, through estimating the rate of battery energy depletion. Two methods are discussed: the basic method minimises the instrumentation required, whereas the improved method reduces the flight test time required at the cost of additional instrumentation, and additional assumptions on battery physical properties.

The basic battery depletion method is perhaps the simplest way to estimate the drag curve of a small, electric UAV. The method consists of estimating the UAV's endurance through repeated energy depletion tests at various cruising airspeeds and relies on an estimate of the efficiency of the powertrain to work out the drag. This method is ideal when a reasonable understanding of the powertrain exists, but there is no means of equipping it with additional instrumentation for more sophisticated testing.

To work out the drag from a single energy depletion flight, the power required for cruising flight needs to be estimated. This is done through the endurance equation derived by [18]:

$$E = \text{Rt}^{1-n} \frac{\eta_{\text{tot}} U_{\text{ave}} C}{P}, \tag{1}$$

where E is the endurance, U_{ave} is the average voltage for the endurance time period, C is the rated battery capacity with a battery hour rating (Rt) value of 1h (thus Rt is 1), η_{tot} is the total efficiency of

the powertrain and P is the power required to maintain the steady level flight. n is the *Peukert* constant, which does not affect the equation due to our assumption of Rt being 1.

In practice, for the basic battery depletion method, the discharged capacity equates to the charge added to the battery as measured by the battery charger, assuming a previously fully charged battery.

After the power is estimated, since $P \approx T V_{TA}$, where P is the power required for steady, level flight (powertrain losses have already been accounted for in Equation (1), T is the thrust and V_{TA} is the true airspeed, the lift and drag coefficients can be calculated by:

$$L \approx W - T \sin(\alpha) \approx \frac{V_{TA}^2 S C_L}{2} \tag{2}$$

$$D \approx T \cos(\alpha) \approx \frac{\rho V_{TA}^2 S C_D}{2} \tag{3}$$

where L is the lift, α is the angle-of-attack, D is the drag, S is the wing area, ρ is the air density and W is the total weight of the aircraft. C_L and C_D are lift and drag coefficients, respectively. C_D can be further decomposed as $C_D = C_{D0} + K C_L^2$ where C_{D0} is the zero lift drag coefficient. K is the lift induced drag constant,

$$k = \frac{1}{\pi \mathcal{R} e}. \tag{4}$$

where $\mathcal{R}$ is the aspect ratio of the aircraft, and e is the Oswald span efficiency.

To generate a complete drag curve, the battery depletion test flight can be repeated at different indicated airspeeds. In addition to the assumptions described in Section 3.2, here we also assume that

- take-off, climb and descent deplete the batteries at the same rate as cruise (a safe assumption in the case of UAVs operating below 400ft)
- the thrust vector is parallel with the axis of symmetry and goes through the centre of gravity
- the discharge current is constant and the battery voltage depletion is slow and steady during the discharge process; therefore, the average voltage can be used for calculations
- the voltage of the battery is related to the charge of the battery
- the Coulombic efficiency is 0.95
- Rt is 1
- the performance of the battery does not change with time

This method can be performed with only a basic manual remote control setup through discharging the battery until the electronic speed controller cuts power to the motor, followed by a dead stick landing. For the purposes of our experiment, a voltage sensor was used to identify a safe end-of-experiment point (short of a full discharge). This end-of-experiment point was chosen so that the battery was not discharged to a dangerous level and allowed for a go-around in case the approach became unstable. In its most basic form, this method is suitable for drag curve estimation. If a lift curve is also required, the angle-of-attack also needs to be estimated.

The accuracy of the drag estimate obtained at the end of the process depends on the ability of the (auto)pilot to maintain a constant altitude and airspeed, while reliably repeating the same circuit, with minimal load factor departures. As the flight is performed at a constant altitude, the climb angle can be assumed to average 0° and hence the pitch angle is sufficient to approximate the average angle-of-attack.

Using an autopilot augmented with the appropriate sensor suite is the most reliable way of flying this method precisely, but it does increase the cost and weight of the components required, which may be significant in the case of very small aircraft (weighing hundreds of grams) designed, for example, to operate as parts of large swarms.

If an airspeed sensor, autopilot and voltage sensor are available, the analysis presented above can be applied to data collected during *segments* of a flight too, flown at different airspeeds. Unlike the basic

version of the method, this improved version does require knowing the state of charge, or having a model to estimate the state of charge at each time step. Each segment of flight assumes that the charge used during the segment is equal to the charge of a virtual battery which is completely depleted during the segment. Thus, the charge at the start and end of each segment needs to be known. We use the polynomial fitting model [19] to model the state of charge of the battery throughout the flight, which expresses the relationship between the change in state of charge and change in voltage.

Knowing the initial charge of the battery and the change in state of charge, the charge used for each segment can then be calculated through an iterative process,

$$Q_i = \frac{\Delta \text{SOC} \, Q_{i-1}}{\eta_{\text{col}}} \tag{5}$$

where Q_i is the charge at time step i, ΔSOC is the change of SOC between time steps i and i $-$ 1, η_{col} is the Coulombic efficiency of the battery.

Following on from here, the Equations (1)–(4) can be used to obtain the lift and drag curve. In addition to the assumptions stated earlier, here we also assume that

- the SOC can be estimated at each time step
- the charge can be calculated from the SOC
- Rt is 1
- the voltage decrease is slow and steady, therefore the average voltage can be used to estimate the endurance for each segment of airspeed

3.2.2 Thrust estimation via voltage and current sensing
Several methods can be applied to calculate the propeller thrust during flight if reliable models and/or performance maps of the components in the powertrain are available. Although we consider only steady level flight conditions (simulating cruise) in this section for simplicity, in reality there is no perfect steady, level, wind-gust-free flight. Therefore, if visual line of sight must be maintained, the test segment should be chosen to maximise the headwind and thus the time in the straight segment. When implemented, the autopilot controls both the airspeed and altitude above mean sea level.

This method estimates the thrust (and thus, implicitly, the drag) by measuring the electrical power output and requires an autopilot, plus airspeed and battery voltage and current sensing capability [2], also applied a similar method by first creating a model of the powertrain efficiency in a wind tunnel and relating the efficiency to the power draw and the airspeed, thus increasing the calculations accuracy. The method implemented in this paper removes this step and thus the need for a wind tunnel test prior to the flight test to reduce the costs involved. The voltage and current sensor method is able to collect data for an entire lift and drag curve in a single flight by flying steady level test segments at different indicated airspeeds, ranging from just above the stall speed to the maximum safe level flight airspeed. The components required for this method are identical to the improved battery depletion method. The sensors record the voltage and current draw of each of the brushless motors for the duration of the flight. The power draw from the battery is calculated as $P = I \, U$ where P is power, I is current draw and U is the voltage. From the assumed efficiency, $\eta_{\text{powertrain}}$, the thrust can be calculated as $T = \frac{P \, \eta_{\text{powertrain}}}{V_{\text{TA}}}$ where T is the total thrust, and V_{TA} is the true airspeed of the UAV. Assuming forces in equilibrium and since the weight is constant for battery-powered aircraft, the lift coefficient, C_L, can be calculated as shown in Equations (2)–(4). The same assumptions apply here as described in Section 3.2.

3.2.3 Thrust estimation from RPM
Propeller rotational speed (RPM) is a useful surrogate for thrust (provided that the performance of the propeller is known). Let us therefore consider some practical direct and indirect methods for estimating RPM in the interest of drawing up the drag curve of an aircraft.
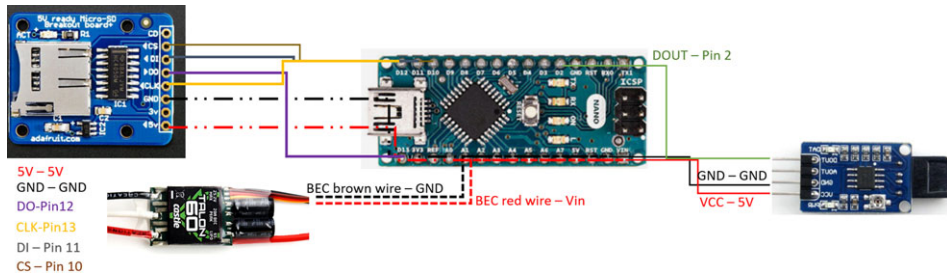
Figure 6. *IR sensor set up.*

Thrust estimation via optical RPM sensing

If the propeller performance map is known, the rotation speed of the propeller, along with the air-speed, can be used to derive a reasonably close estimate of the thrust generated by the propeller (with possible errors due to integration effects and propeller performance in-service degradation). If the propeller is directly attached to the motor shaft (as is the case with most small UAVs), the rotation speed of the propeller is the same as that of the rotor of the electric motor. Therefore, an optical tachometer based on an infrared (IR) sensor, a laser sensor, a Hall effect sensor or photo-interrupter can be used to measure the rotation speed of the propeller.

The test platform used in the experiments described in this paper (FliTePlat) is equipped with an IR sensor. It uses an LED, which emits IR waves towards the rotor of the electric motor. These get reflected by a reflective strip on the surface of the motor and are sensed by a photodiode. The sensor is paired with an onboard micro-controller, which reads the number of pulses that the photodiode detects, calculating the RPM and storing the values on an SD card. Once the thrust has been interpolated from the propeller performance map, the derivation of the lift and drag curves is trivial (Equations (2) and (3)).

The hardware setup is relatively simple (see Fig. 6 for an example implementation). The IR sensors are sensitive to daylight; they can be shielded from background IR radiation by embedding them inside the motor housing. Since the electric motor requires high current, the signal wires may require electromagnetic shielding in some installations.

Once again, automated (autopilot-flown) versions of this thrust/drag estimation method are likely to yield more accurate results, especially in relatively gusty conditions.

Thrust estimation through audio-derived RPM measurements

An unobtrusive method for measuring the rotational speed of the propeller is the use of audio. By obtaining the fundamental frequency via spectral analysis, the motor rotation speed can be estimated and thrust and drag can then be calculated as before.

The key advantage of this approach is that there is no mechanical contact between the motor and the sensors; indeed, the latter do not even need to be near the powertrain (unlike the methods described above). An additional benefit is that the audio device acts as a cockpit voice recorder, which can be used to identify exact timings of various in-flight events (servo operation, sounds of relays, sparks), intended or anomalous (or, indeed, may help identify the anomaly itself).

The downside is the relatively time-consuming post-processing; this is due to the relatively large bandwidth required (typically up to 44kHz). Figure 7 is an example of a frequency map recording during a takeoff segment, showing an estimate of the propeller rotation speed extracted from the data. We have deliberately chosen an unusual example here: the aircraft sustained a propeller strike during the take-off roll on this flight. The result is reflected in Fig. 7, where an abrupt drop is visible around the 6s mark. However, this plot also demonstrates the main difficulty with estimating the propeller speed using fundamental frequency estimation without sophisticated data post-processing: erroneous readings can be seen about 2s in and around the 8s mark.
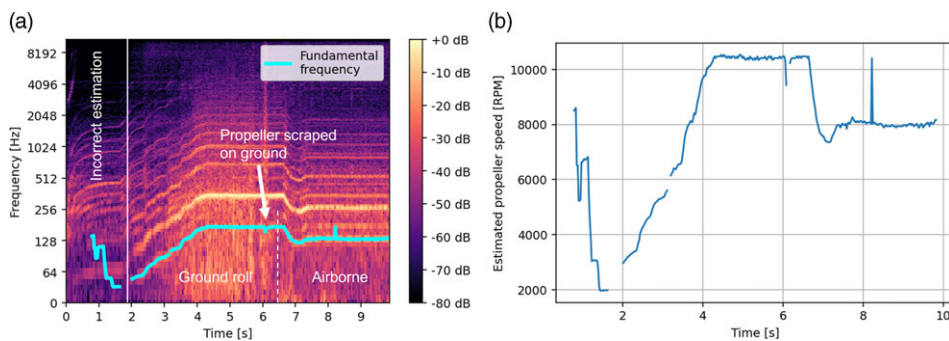
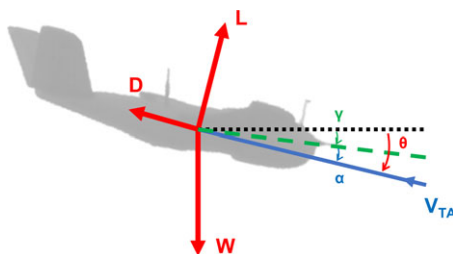**Figure 7.** *Propeller speed extraction from audio data.*

Figure 8. *Forces acting on the UAV during gliding flight.*

An advantage of audio-based RPM measurement (in addition to the general data-richness and related serendipitous uses of the recording) is the freedom in terms of siting the sensor (this could be important if the test engineer has limited re-design authority on an existing platform). Indeed, on FliTePlat, the audio recording module is used as a centre of gravity tuning mechanism, allowing the use of a wider range of battery sizes.

3.3 Unpowered flight test methods

3.3.1 Manual glide slope method

The manual glide slope method has been used extensively due to its simplicity [10, 11]. The idea is to observe the climb (descent) angle $\gamma = \arcsin\left(\frac{dh}{dt}/V_{\text{TA}}\right)$ (see Fig. 8) in a descent flown at a known weight W. The lift and drag can then be estimated as $L = W\cos\gamma$ and $D = -W\sin\gamma$. Glides are flown at a set of true airspeeds spanning the range between the stall speed, V_{S}, and the maximum dive speed, V_{D}. The result obtained at each speed can either be an estimate based simply on the end states of the glide [11], or can be calculated at each time-step recorded throughout [10].

The advantage of the manual glide method, compared to some of the automated approaches we are about to discuss, is that it can be performed with basic instrumentation and does not require a fully functional autopilot, thus reducing the equipment cost and additional mass involved.

3.3.2 Automated glide slope method

Like the methods discussed above, glide slopes flown at multiple airspeeds also benefit from automation (largely because they remove error dependence on operator skill). Moreover, the automation of the off-line processing of the data it generates can pay accuracy and workload dividends, especially after high-resolution airspeed sweeps (see Ref. (20) for an example of a suitable flight data batch analysis and
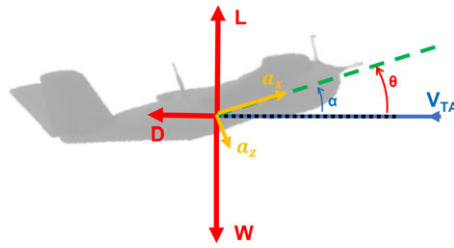
Figure 9. *Forces and accelerations acting on the UAV during the slow down manoeuvre.*

summarisation tool). The method is automated through setting the desired glide airspeed as the cruise indicated airspeed and adjusting the total energy control system to maintain the indicated airspeed and disregard any errors between the target altitude and the actual altitude. The total energy control system is a control algorithm implemented by the autopilot to maintain a constant total energy (kinetic + potential). This is done through varying the throttle and pitch to control the airspeed and altitude. At the initiation of the gliding segment, the throttle is set to zero, forcing the autopilot to sacrifice altitude to maintain the cruising indicated airspeed via appropriate deflection of the ruddervator. These autopilot changes were implemented through the use of a Python script that monitored the current position and state of the UAV.

As opposed to the manual glide slope method, this method requires automatic flight capabilities, raising the cost and component count.

3.3.3 Lift and drag estimation via slow down manouvres

The glide slope method discussed above essentially estimates the amount of work done by the drag in depleting the potential energy of the unpowered airframe. An alternative approach is to allow the drag to deplete the kinetic energy of the aircraft by entering the testing segment close to the maximum level flight airspeed, cutting the power and allowing the UAV to decelerate in level flight. This involves increasing the angle-of-attack as the aircraft slows down, sweeping through the entire angle-of-attack range in a single manoeuvre. This manoeuvre has the added advantage of providing the test operator with the indicated stall airspeed, if needed. Slow downs can be repeated several times to increase the curve estimation confidence.

This manoeuvre, similar to the automated glide slope manoeuvre, takes advantage of the total energy control system. Here, the UAV is first commanded to fly at the maximum level flight indicated airspeed and, upon manoeuvre entry, the throttle is set to zero and the total energy control system is commanded to maintain altitude via appropriate ruddervator deflections and ignore any airspeed errors between the target indicated airspeed and the measured indicated airspeed.

Figure 9 presents the forces and accelerations acting on the UAV throughout the slow down manoeuvre. As the accelerometers on-board are only measuring the accelerations due to aerodynamic forces. The lift and drag can be calculated as 6 and 7.

$$L = m \left(a_x \sin\alpha - a_z \cos\alpha + V_{TA} \frac{d\gamma}{dt} \right) \tag{6}$$

$$D = m \left(-a_x \cos\alpha - a_z \sin\alpha \right) \tag{7}$$

where a_x and a_z are the body accelerations in the x and z axes. Note the inclusion of acceleration due to turning flight about the y axis in the lift equation, this term is included as the manoeuvres are never performed with ideal accuracy.

While the sweeping of the full angle-of-attack range in a single manoeuvre is quite economical, slow down segments will require time and space for building up the required entry speed. Also, once again,

Figure 10. *RAPTA UAV with thrust and angle-of-attack measurement capabilities.*

extensive autopilot sensing capabilities are required to continuously record the indicated airspeed, body axis accelerations and pressure altitude throughout the manoeuvre. The angle-of-attack can either be measured directly or calculated from the climb angle and the pitch angle. Although the manoeuvre can be flown manually, an automated flight plan results in higher accuracy and repeatability and, given that the autopilot's data logging capabilities and sensors are already required on-board the UAV, we only consider this manoeuvre in an automated flight context.

3.4 Additional methods

These methods are described for completeness but have not been implemented by the authors on FliTePlat due to their respective limitations.

3.4.1 Measuring thrust directly

If weight restrictions and size restrictions allow, a load cell can be integrated into the motor mount, allowing for direct measurement of thrust. A load cell conditioner and amplifier device are used to generate a force signal.

It is straightforward to generate a complete curve once load cells have been fitted. The UAV can be flown at different airspeeds whilst recording the angle-of-attack. Equations (2)–(3) apply for level flight, although this is not a requirement for this method.

In general, a disadvantage that sets this method apart from those discussed earlier is that retro-fitting the required sensing capability to an existing aircraft is almost always quite invasive; even in the case of *ab initio* integration, the design of the load cell can end up compromising the design of the propulsion system itself.

Consider, for example, the RAPTA UAV (Fig. 10), featuring a turbojet engine pylon-mounted on a load cell, above the fuselage. Unlike an integrated turbine installation, this choice (driven by the need expressed in the design brief to install a load cell) resulted in a substantial pitching moment generated by the thrust, as well as additional drag. This layout also forced a shallow v-tail design in the interest of keeping the tail out of the jet wash. Moreover, the pylons, the sensors and the associate auxiliary equipment may involve a non-trivial mass increase, especially in the case of multi-engined aircraft. Another disadvantage of the load cell method is the measured noises [5]: vibration from the sensor itself – especially as the load cell is mounted directly on the source of the vibration (engine/motor), external vibrations of the vehicle, and the effect of propeller and fuselage wake interaction all contribute.
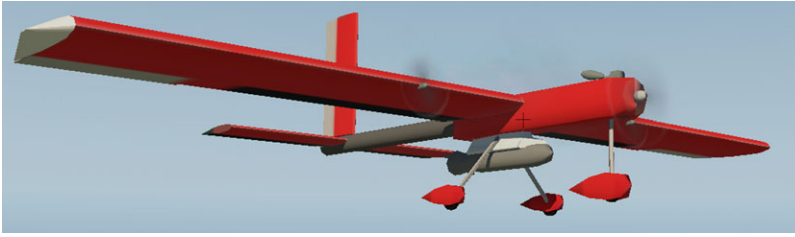
Figure 11. *PEREGRIN UAV simulated in the X-Plane 11 environment.*

Other examples of direct thrust measurement applications include Lemke et al. [21], whom implemented a displacement transducer, and McArthur [22], whom used a strain gauge and accelerometer setup to estimate transient thrust properties. Notable mounting mechanisms of load cells on electric powered UAVs are hinge type and linear bearing type mounts. Gong et al. [6] used a hinge type for mounting the thrust cell on a twin-engine RC model Cessna 310 to test level acceleration, straight and level flight and unpowered glides. Bergmann et al. [3] and Pfeifle et al. [4] used a force sensor with a linear bearing mount on the motor of a 33.3% scaled electric e-Genius aircraft to test steady horizontal flight and generic flight conditions, respectively.

3.4.2 Camera tracking

The camera tracking method has been included for completeness and has not been investigated using FliTePlat due to limitations at the scale of interest. Camera tracking requires several cameras to be set up and calibrated around the test area. An object (in our case, a UAV) is then flown through the test area and, using the 3D tracking, the accelerations and hence forces can be calculated. Mettler [23] and Uhlig and Selig [24] used this method for micro air vehicles in gliding flight with Uhlig and Selig [24] expanding this to powered flight. For larger UAV such as FliTePlat, an outdoor camera system would be required. This is, however, comes with the major drawback as the method cannot account for the windspeed and direction.

The camera method requires multiple specialised cameras to be set up around the testing volume and passive infrared tracking markers positioned around the target object. The *University of Southampton*'s engineering department has access to a six camera setup on which the following information is based. The tracking system is accurate at tracking the motion of the markers down to 0.1mm and runs at a typical frequency of 300Hz. The imaging frequency can be increased although, as processing is done by the cameras, this results in a reduction in the usable test area.

3.4.3 Digital flight testing

There is an increasing range of digital alternatives to the flight test methods reviewed above. They span a broad range of costs, with high fidelity Reynolds Averaged Navier Stokes (RANS) or full-potential flow solvers at one end, to blade element theory (BET)-based methods at the other. The latter is perhaps the most attractive option in the world of small UAV platforms, due to the low costs involved (both in terms of software and training needed), and due to the additional benefit of it affording insights into the handling characteristics of the aircraft (beyond basic performance estimates, such as those we are concerned with here).

One of the most widely used such tools is X-Plane 11 [25], which allows the relatively easy definition of the geometry of the airframe [26], with the lift and drag of the lifting surfaces approximated in 2D and the drag of the non-lifting surfaces, such as the fuselage, spats, and engines, modelled through an incremental drag method (e.g. Fig. 11). The dynamics of the aircraft is then approximated using a BET-based model [27]. Of course, the performance figures (including lift and drag) obtained in this way come

Method \ Components	RC setup	Flight computer	Data acquisition system	Telemetry module	GNSS Receiver	Basic airspeed system	Advanced airspeed system	Basic voltage sensor	Advanced power sensor	Basic variometer	Infrared proximity sensor	Audio system	Relative mass of the required components
Basic battery depletion (manual)	■					■		■					▏
Basic battery depletion (autopilot)	■	■	■	■	■	■		■					▆
Improved battery depletion	■	■	■	■	■				■				▆
Thrust from voltage and current	■	■	■	■	■				■				▆
Thrust estimation from infrared sensor	■	■	■	■	■						■		▆
Thrust estimation from audio sensor	■	■	■	■	■							■	▇
Manual glide slope	■					■				■			▏
Automated glide slope	■	■	■	■	■	■							▆
Automated slow down	■	■	■	■	■	■							▆

Figure 12. Relative equipment requirements for each method.

with accuracy-related caveats, not least due to the limitations in terms of capturing the subtleties of the 3D features of the airframe.

3.5 Relative equipment requirements

Each method discussed in this section comes with different equipment requirements. Figure 12 summarises these, along with their relative cumulative component masses; though these need to be considered with the health warning that they are somewhat implementation- and application-dependent, and that some methods have practical advantages that may negate the additional on-board mass. For example, a microphone and a sound card may be an apparently heavy means of estimating motor speed, but the setup can be made electronically and mechanically independent of the rest of the airframe; in general, non-intrusive sensing is a hard to quantify, but sometimes very effective element of a good flight test strategy, especially on legacy systems that may require re-certification of the airworthiness after the installation of more tightly integrated instrumentation.

4.0 Results and discussion

Having compared the equipment requirements of the methods and their respective mass penalties, let us now discuss the relative accuracy of the methods. The following section presents and analyses the lift and drag curves generated via each method in turn. We then compare the data to a wind-tunnel-generated baseline, taking into account sources of errors, and a selection of optimal manoeuvres are defined. We then conclude by combining the optimal manoeuvres into a set of optimal strategies, taking into account the weather conditions and the flight testing time available.

4.1 Wind tunnel testing

In order to serve as a reference for the scatter of the data for the manoeuvres investigated, Fig. 13 shows the data collected on FliTePlat through a test campaign at the *R.J. Mitchell* wind tunnel, investigating the drag of the airframe in different configurations. Each point represents data taken at a sampling rate of 1kHz, averaged over 20s. This data also highlights the effect of stationary propeller position on the drag

Table 2. *Comparison of coefficients generated through different methods with reference to the wind tunnel data.*

Method	C_{D0}	K	C_{L0}	$C_{L\alpha}$ [1/deg]
Wind tunnel test (reference)	0.0503	0.0764	0.2570	0.1122
Battery depletion – basic method	0.0327	0.1787	0.2882	0.0920
Battery depletion – improved method	0.0204	0.1377	0.2871	0.0757
Voltage and current sensors	0.0372	0.0994	0.3820	0.0577
Thrust estimation from RPM	0.0317	0.0998	0.3719	0.0583
Manual glide slope (based on 7 glides)	0.0149	0.1548	0.2195	0.0414
Automated glide slope (based on 9 glides)	0.0552	0.0686	0.3242	0.0725
Automated slow down (based on 10 manoeuvres)	0.0526	0.0784	0.3158	0.0704
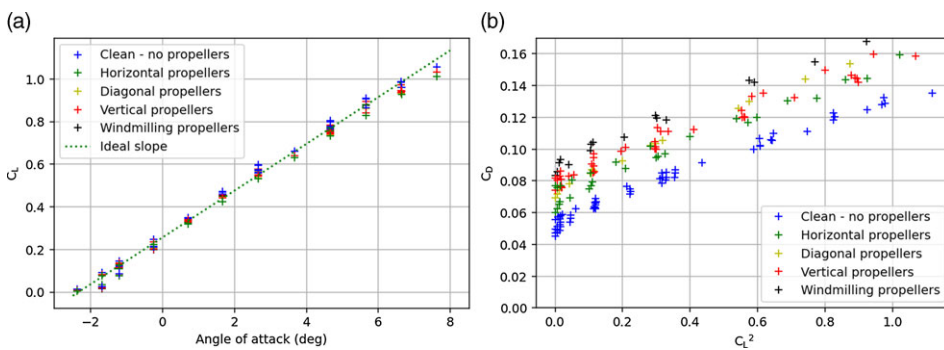
Figure 13. *FliTePlat lift and drag obtained in the wind tunnel.*

coefficients, with the vertical, horizontal and diagonal propeller position data spanning around 20% of the average C_D (we have also included the 'no propellers' and 'windmilling propellers' cases to serve as extreme reference values). The propeller position is typically not controllable for unpowered methods (such as the glide slope and slow down methods) and results in potentially significantly different drag coefficients.

The coefficients are extracted through linear regression through both the lift and drag data, with the intercept being the zero angle-of-attack lift coefficient and zero lift drag coefficient, respectively, and the resulting gradients being the lift curve slope and the lift induced drag constant. As the wind tunnel data is collected in ideal test conditions, there is little noise present in the data. The coefficients are presented in Table 2.

The data presented here serves as a 'clean' baseline (rarely achievable through flight testing). The following section compares this to the equivalent data collected through powered and unpowered flight testing. This also serves to compare the flight test methods with one another in order to assess not only the spread of the data but also the angle-of-attack range covered through each manoeuvre.

4.2 Battery depletion methods

The experimental process for calculating lift and drag via the basic battery method consists of flying a fixed altitude mission at a fixed airspeed, while monitoring the battery voltage (this continuous voltage monitoring and thus performance assessment increases the efficiency of data acquisition compared to unpowered manoeuvres, though generally at the expense of the breadth of the angle-of-attack coverage). For greater accuracy and repeatability we flew the automated version of the manoeuvre to obtain the
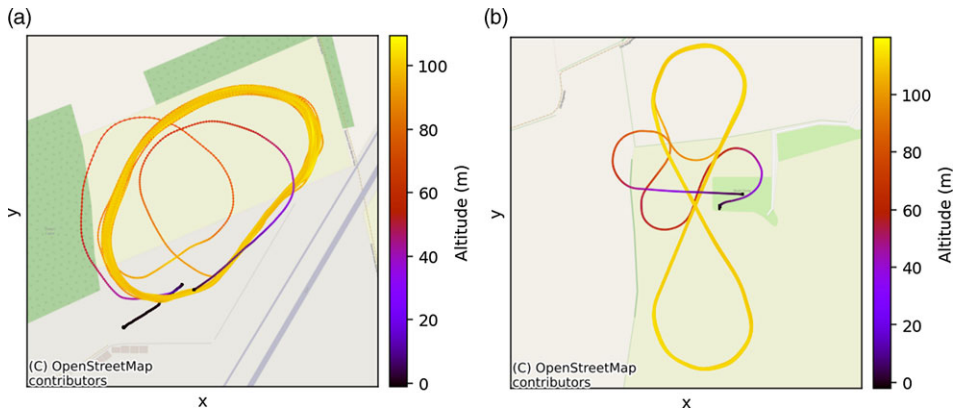
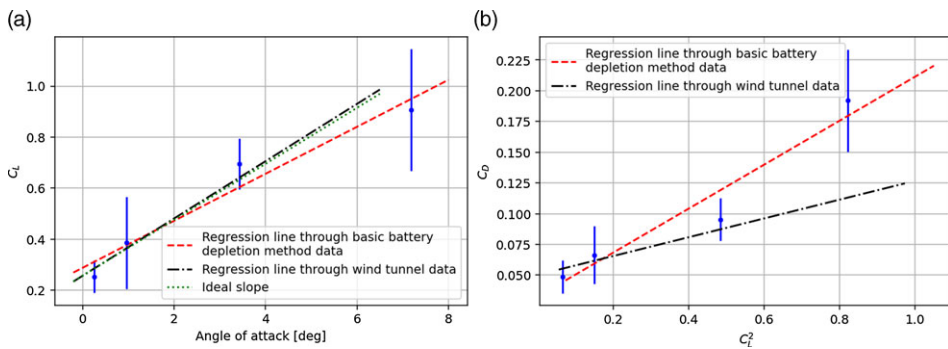**Figure 14.** *Different flight paths for endurance testing.*

Figure 15. *Lift and drag curves estimated via the basic battery depletion method.*

results shown here; nevertheless, the resulting zero lift drag coefficient was still a substantial under-estimate of that obtained from the wind tunnel data. Part of the suspected reason for this (and for the inaccuracies of the method in general) is that visual line of sight rules mean that the aircraft spends much of the flight time manoeuvring, whereas the calculations assume level flight. Figure 14 shows two typical flight test paths, with (a) maximising the turn radius subject to environmental constraints, and (b) maximising the linear segment length at the cost of a tighter turn radius.

Figure 15 presents the lift and drag curves calculated through four battery depletion flights flown with cruise speeds of 13, 15, 20 and 25m/s, respectively. These flights lasted between 42 and 116min (these duration being an additional reason why manual depletion tests are generally not practical). The angle-of-attack range that can be covered through this method is limited to angles of attack typical of the practical cruising speed range of the aircraft.

Another drawback is the reliance on generic state of charge models. Moreover, the powertrain efficiency is estimated based on legacy data, which generally does not account for ambient temperature and battery age effects.

Similarly Fig. 16 shows the lift and drag curves calculated through two separate flights, both with indicated airspeeds ranging from 13 to 30m/s. The lift curve slope is lower than for the wind tunnel regression which increases the gradient of the drag curve. Both the basic battery depletion method and the improved battery depletion method shows the same trends when compared to the wind tunnel regression data. Due to the shorter flight times involved in the data gathering for the improved battery depletion method when compared to the basic battery depletion method, a larger angle-of-attack range
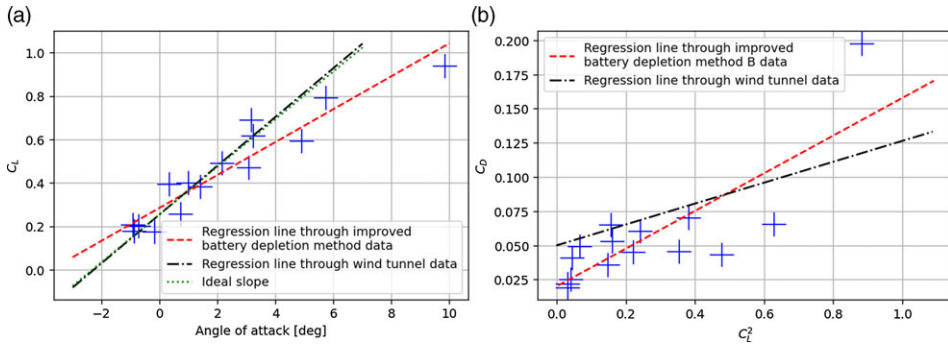
Figure 16. *Lift and drag curves estimated via the improved battery depletion method.*

Figure 17. *Flight path for thrust estimation methods.*

can be covered. However, as the drag curve shows, the method is susceptible to noise in the data, and systemic errors such as voltage recovery in the battery when transitioning from high airspeed flight to lower airspeed flight.

Flying multiple flight segments with varying airspeeds assumes that each segment is flown using a battery with the capacity equal to the energy expended during that segment. The data was analysed first by estimating the SOC based on Zhang et al. [19], then the charge using the Equation (5). The true airspeed dependency of the powertrain efficiency must also be taken into account. Another challenge in implementing this method is the voltage recovery during the flight, when moving from high current draw at high airspeed to low current draw at low airspeed [28]. Finally, the precision of commercial-off-the-shelf sensors is also an important factor as the results are based on the recorded voltages at each point.

The mission used to collect data using thrust estimation based techniques (via voltage and current sensing and via RPM) included flying the test segment at different indicated airspeeds. The flight pattern can be seen in Fig. 17. These flights were automated and lasted between 19 and 24min. Unlike in the wind tunnel, this set of experiments requires power-on flight; therefore, the propeller slipstream increases the airflow speed over the wings, affecting the lift. Moreover, wind tunnel experiments are conducted in ideal condition, whereas flight testing is susceptible to environmental conditions such as gusts and errors in flight control inputs.

Figure 18 presents the lift and drag curves calculated through two flights with test segments at a range of different indicated airspeeds. The data presented in Fig. 18 covers the indicated airspeed range
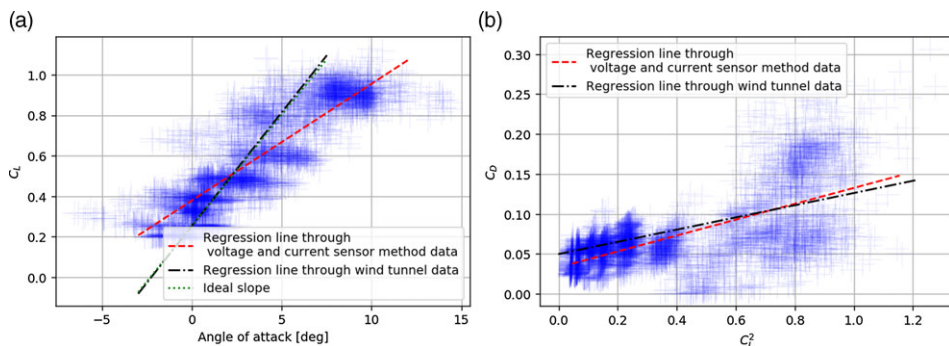
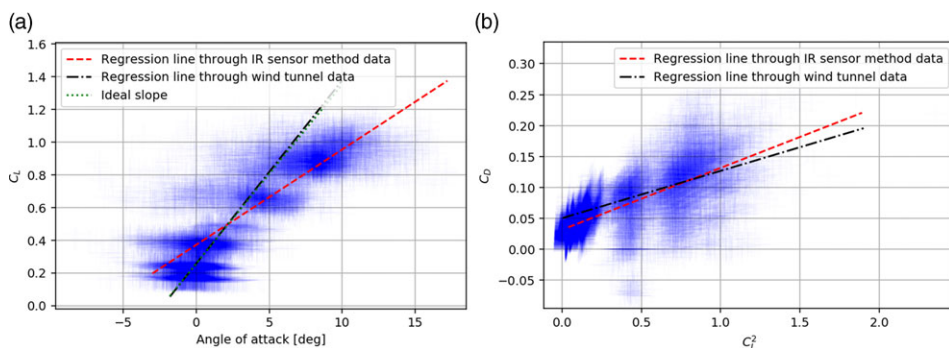**Figure 18.** *Lift and drag curves calculated from voltage and current sensors onboard.*

Figure 19. *Lift and drag curves for thrust estimation using IR sensor.*

between 13 and 30m/s. The lift curve shows a linear trend, with C_{L0} overestimated and $C_{L\alpha}$ underestimated with respect to the wind tunnel lift curve. This effect is carried on to the drag curve with C_{D0} vastly underestimated compared to the wind tunnel data.

A main source of error for this process comes from estimating the propeller's performance. When propeller data are not available, blade element momentum theory [29] (through software such as pyBEMT by Giljarhus [30]) can be used for estimating the performance curves (thrust, torque, power and efficiency) of a known propeller with known geometry such as the radius, number of blades, blade chord, aerofoil section shape and twist distribution. In this work we employed the performance data provided by propellers [31]. Since the propeller data here is obtained from the manufacturer [31] as a table of discrete steps of propeller speed, it is necessary to interpolate the data into a propeller map. Throughout the same flight presented in Fig. 17, the motor RPM and the audio data were recorded. As both of these methods rely on broadly the same analysis process, once the motor RPM were determined, a set of lift and drag curves were derived. The results of the thrust estimation from propeller maps, motor RPM and the airspeed are presented in Fig. 19. These curves exhibit largely the same discrepancies with respect to the wind tunnel lift and drag curves as seen in Fig. 18.

4.3 Averaged glide slope curves – manual and automated

The data presented here was generated with FliTePlat's propellers electrically locked, on two different days. The manual glide slopes were preformed by an experienced UAV test pilot following the process described in Section 3.3.1 with the automated glide slopes following the method described in Section 3.3.2.
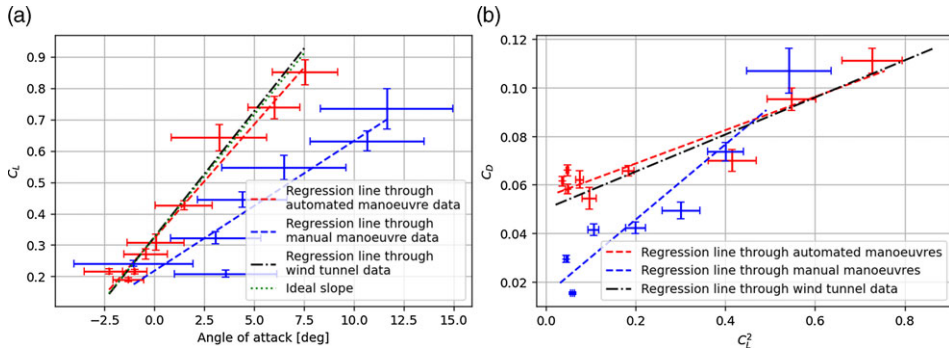
Figure 20. *Glide slope manoeuvre derived lift and drag, with $\pm$ one standard deviation error bars.*

Figure 20 represents the lift curves generated by the manual and automated flights, both analysed by averaging the data over each glide slope. As can be seen, the automated manoeuvre's error bars are smaller than for the manual manoeuvres, thus demonstrating the piloting improvement gained through automating the manoeuvre, especially at high indicated airspeed glides (low angles of attack). The two resulting curves are significantly different, with the least squares fit resulting in a C_{L0} of 0.2195 and 0.3242 for the manual and automated manoeuvres, respectively. Figure 20 represents the drag curves generated from the data. This varies substantially more than the lift curve, however, the C_{D0} generated through automated manoeuvres is 9.69% away from the wind tunnel data, whereas the C_{D0} generated through manual manoeuvres is 70.37% out, demonstrating the increased accuracy of the automated manoeuvres over the manual manoeuvres (re-iterating the caveat that the wind tunnel derived reference data itself may be subject to its own offsets from 'reality', but it is much more repeatable than individual flight tests). For comparisons of the remaining coefficients generated through these manoeuvres with the wind tunnel coefficients, see Table 2.

Limitations of this method include the loss in altitude throughout and, as for all unpowered methods, the need for a rapid restart capability at the end of the glide. In the UK, visual line of sight regulations limit UAV flight to a maximum altitude of approximately 120m. Factoring in the altitude required for recovering from the glide in a safe manner, this limits the typical manoeuvre altitude change available to around 70m. At an indicated airspeed of 27m/s, typical for the low end of the angle-of-attack spectrum in the case of FliTePlat, this limits the data collection time to 10s or so, with corresponding limitations in terms of accuracy. Due to the high descent rates, this method also carries considerable risk and potential loss of the airframe in case the recovery is not initiated in time. For combustion engine powered UAVs the method either needs to take into account the additional drag from an idling engine, or each glide has to end in a dead-stick landing which limits the practicality of the method.

4.4 Slow down manoeuvre

The slow down manoeuvre described in Section 3.3.3 was repeated ten times in order to reduce the errors caused by gusts. The lift and drag curves are presented in Fig. 21. Note the high angle-of-attack range achieved with this method – this is enabled through the high indicated airspeed range between the maximum level flight airspeed and stall. The data follows similar trends to the automated glide slope method.

This manoeuvre is very constrained by the 500m radius of visual line of sight regulations as both the acceleration to entry velocity and slow down to stall need to be performed on the same straight segment. Another issue here (shared with the descent-based methods) is that of the propellers stopped in an unknown position, adding an unknown drag increment. This method also relies on a correctly tuned autopilot, which needs to perform the manoeuvre smoothly, while maintaining altitude. The manoeuvre
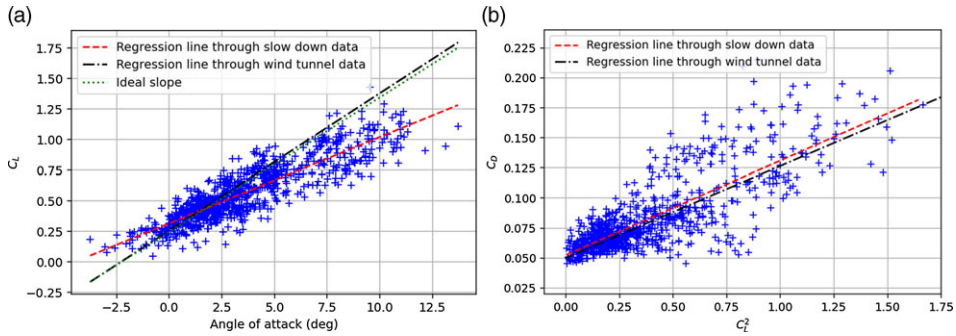
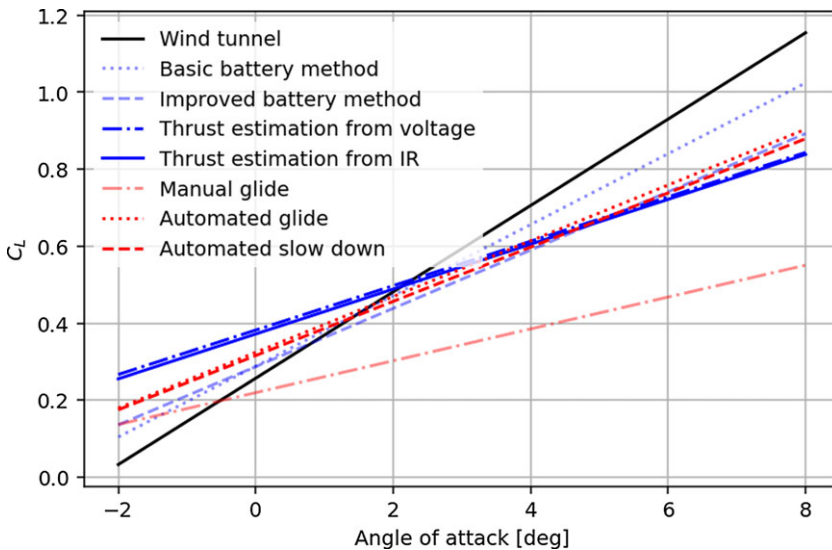***Figure 21.*** *Lift and drag curves for ten slow down manoeuvres.*

Figure 22. *Lift curve slope comparison for different methods.*

also carries risks in case the autopilot fails to recover from the stall or recovers in a manner that exceeds the airframe's maximum load factor, leading to potential damage to or loss of the airframe.

4.5 Method comparison summary

Table 2 summarised the data collected through the methods above, where applicable. An interesting observation to make here is that the lift curve slopes for all flight test methods presented are consistently lower than the wind tunnel data, suggesting that the aerodynamically clean conditions in the wind tunnel do not accurately represent the effect of atmospheric conditions at this scale. The increased lift curve slope from the wind tunnel data may also be due to the effect of the wind tunnel mount used, which consisted of sheet steel aligned with the airflow. This could have acted as a wing fence, segregating the low pressure region above the wings from the fuselage. Nevertheless, the wind tunnel coefficients are still a good comparative reference to the flight test methods.

Figure 22 represents the lift curves obtained through the different methods. We plotted the results of all the methods we have tested, though some may be disregarded for practical reasons. These are the manual glide method, which is an inferior version of the automated glide slope method, and the two

Table 3. *Comparison of the predicted performance of aircraft with the coefficients from Table 2 with reference to the wind tunnel data.*

| Method	$\left(\dfrac{L}{D}\right)_{MAX}$	$Range_{MAX}$ [km]	$Endurance_{MAX}$ [min]
Wind tunnel test (reference)	8.07	114	157
Battery depletion – basic method	6.54	92	92
Battery depletion – improved method	9.43	133	127
Voltage and current sensors	8.22	116	139
Thrust estimation from RPM	8.89	126	144
Manual glide slope (based on 7 glides)	10.41	147	125
Automated glide slope (based on 9 glides)	8.12	115	164
Automated slow down (based on 10 manoeuvres)	7.77	110	151
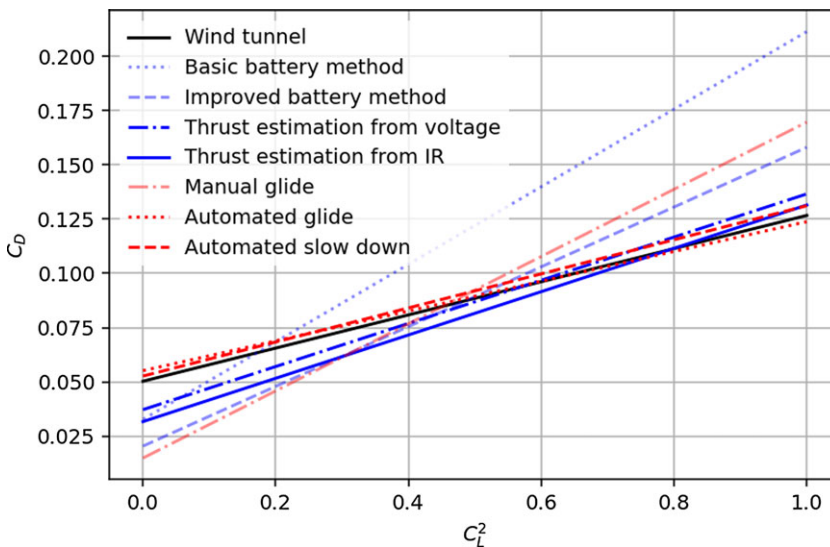
Figure 23. *Drag curve slope comparison for different methods.*

battery depletion methods which rely on over-simplified models and assumptions and are not as accurate as the thrust estimation methods.

There are clear distinctions between the power-on methods (blue) and the unpowered methods (red) which become apparent here. The power-on methods have a higher C_{L0} than the unpowered methods due to the additional airflow over the wings generated by the propellers and the potential flow disruption present in the unpowered methods as a result of a stationary propeller. Figure 23 represents the equivalent drag curves. Here it is clear that the unpowered methods yield a higher C_{D0} than the power-on methods due to the additional drag of stationary propellers of various orientations. During prior wind tunnel testing we found that this difference can range between 0.01 and 0.03 C_D for FliTePlat for horizontal and vertical propellers, respectively, which is consistent with the difference in C_{D0} seen here.

So what is the practical impact of the deviations observed here, in terms of engineering and operations? Using the coefficients from Table 2 where applicable, the ideal range and endurance for FliTePlat can be calculated using the electric Brequet range and endurance equations [32]. Table 3 summarises the predicted performance calculated from the coefficients in Table 2.

The recommended power-on methods are the voltage and current method and the thrust estimation from RPM sensors. These methods do, however, rely on an estimated powertrain efficiency for the former
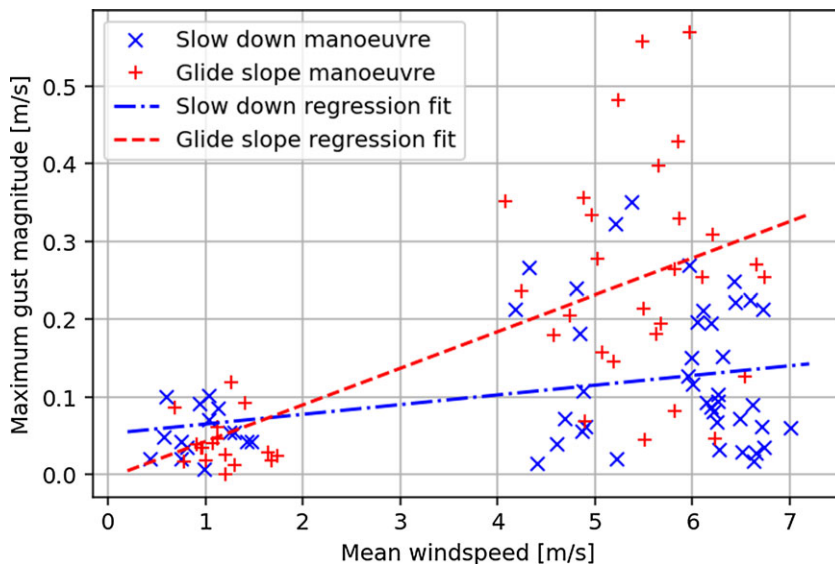
Figure 24. *Maximum gust speeds experienced during automated glide slope and slow down manoeuvres.*

and a reliable propeller map for latter. For unpowered methods, both the automated glide slope method and the automated slow down method provide promising coefficients with the additional drag and airflow disturbance of the stationary propellers.

At this point the reader may be wondering why the battery depletion method is not seen as the best way of estimating endurance/range (after all, both figures imply flying the aircraft to battery depletion). There are two practical reasons for this. On the one hand, flying to 0% state of charge is likely to cause damage to a potentially expensive battery or, at the very least, to affect its capacity from one test flight to the next (leading to a decline in performance through the test). The other disadvantage of simply flying to depletion (when compared to those methods that yield a more accurate estimate of the drag coefficients) is that the results thus obtained cannot be extrapolated to different mission profiles (for example ones requiring multiple climb and descent segments). Thus, the range and endurance figures shown in Table 3 should simply be read as more convenient, intuitive numbers to compare than the aerodynamic coefficients they were derived from, rather than specific estimates of range and endurance.

4.6 Manoeuvre strategy optimisation

The automated, unpowered glide and slow down methods emerge from the foregoing as having a number of practical advantages, as well as reliable accuracy. We have also found that their practical usefulness may depend on the specific environmental conditions on the day and that each has its drawbacks and pitfalls. All this raises the question of how one might construct a robustly accurate test campaign that mixes these two methods in an optimal way, for example to maximise the accuracy of the estimates of aerodynamic coefficients within a given time budget.

In this section we will answer this question using data obtained through 45 glide slope and 55 slow down manoeuvres, flown over a single multi-day flight test campaign using FliTePlat.

The flights were performed in two distinct sets of weather conditions (Fig. 24), characterised by wind speeds below 2m/s and above 4m/s, respectively. From Fig. 24 it is clear that the automated glide slope and slow down manoeuvres experience different gust magnitudes associated with various mean
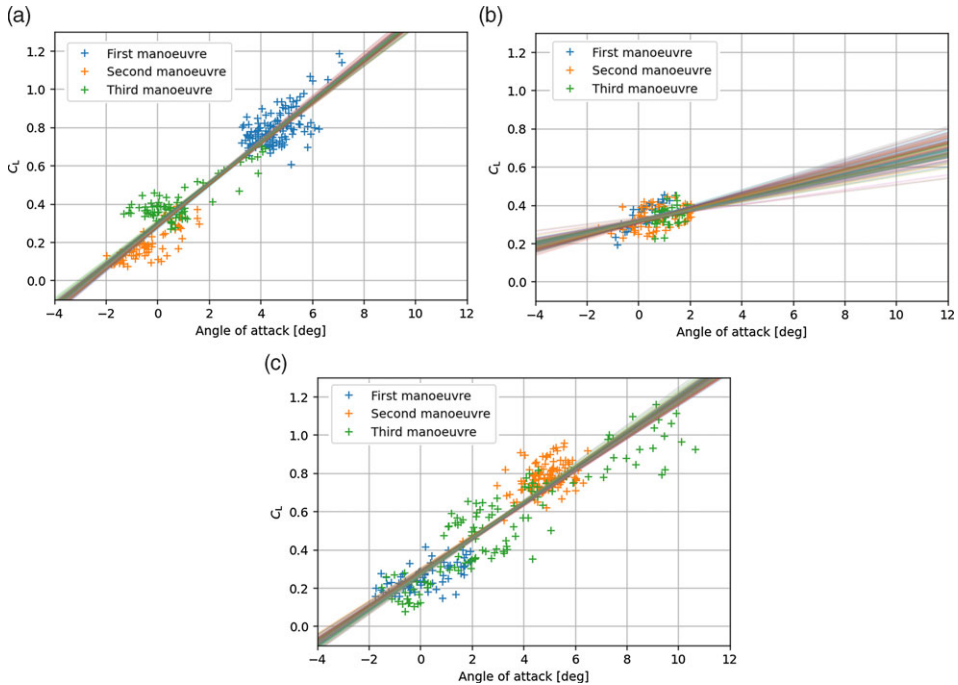
Figure 25. *Lift curves demonstrating the importance of having a good spread of glide airspeeds and the benefits of combining manoeuvres.*

windspeeds. This is due to the fundamental differences between the two manoeuvres – the automated glide slope method involves descents through the atmospheric boundary layer, whereas the slow down method is performed at a constant altitude. Further, the glide slope manoeuvres may take longer to complete, which likely explains the greater scatter of the '+' points on the figure.

In what follows, we shall examine a range of strategies, that is, combinations of glide descents and slow down segments. Each individual strategy (combination of descents and slow downs) is evaluated to generate a set of lift and drag coefficients (C_{L0}, $C_{L\alpha}$, C_{D0} and k) from the data observed during these manoeuvres. We employ a Monte Carlo approach here, which, at each iteration, randomly samples (with replacement) half of the data points, and calculates the coefficients corresponding to this subset (bootstrapping [33]). We perform 100 such iterations to generate a set of sets of coefficients (100 sets of C_{L0}, $C_{L\alpha}$, C_{D0} and k), which enables calculating a mean and a standard deviation for each coefficient. Taking three manoeuvres as an example (Fig. 25), these can either consist of three glide slope manoeuvres ((a) and (b)), three slow down manoeuvres or a combination of manoeuvres (two slow down and one glide slope or one slow down and two glide slope (c) manoeuvres). Additionally to selecting the combination of glide slope and slow down manoeuvres, the glide slope manoeuvres require a good range of airspeeds to increase their coefficients' accuracy as is evident through comparing Fig. 25 ((a) and (b)). Hence, in choosing an optimal strategy for each number of manoeuvres available, it is important to determine both the combination of glide slope and slow down manoeuvres as well as the indicated airspeeds for the glide slope manoeuvres.

As a 'ground truth' for comparing various subsets, we used the data collected from all 100 automated glide slope and slow down manoeuvres. This is used to work out a normalised mean error between the mean coefficients generated from the Monte Carlo simulation and the 'true' coefficients.

The objective function chosen for this task is a combination of the weighted sum of the error in the mean and combined standard deviation. The error in the mean requires a ground truth coefficient set

to be known, used to calculate the difference of each coefficient in the subset to the accepted mean. The errors are then normalised by the accepted mean value for each coefficient and summed to provide an indication of the accuracy of the lift and drag curves:

$$\hat{\mu}_{e,i} = \frac{C_{D0,i} - C_{D0,\text{true}}}{C_{D0,\text{true}}} + \frac{k_i - k_{\text{true}}}{k_{\text{true}}} + \frac{C_{L0,i} - C_{L0,\text{true}}}{C_{L0,\text{true}}} + \frac{C_{L\alpha,i} - C_{L\alpha,\text{true}}}{C_{L\alpha,\text{true}}},$$

where $\hat{\mu}_{e,i}$ is the mean error for coefficient set i.

The standard deviation is, similarly, normalised by the accepted coefficients and is then summed,

$$\hat{\sigma}_i = \frac{\sigma_{C_{D0,i}}}{C_{D0,\text{true}}} + \frac{\sigma_{k,i}}{k_{\text{true}}} + \frac{\sigma_{C_{L0,i}}}{C_{L0,\text{true}}} + \frac{\sigma_{C_{L\alpha,i}}}{C_{L\alpha,\text{true}}},$$

where σ is the standard deviation of the respective coefficient and $\hat{\sigma}_i$ is the summed normalised standard deviation of the strategy.

The weighted objective function used to compare different strategies equally considers the sum of the normalised mean error and sum of the normalised standard deviation. The sum of the normalised mean error represents a measure of the accuracy achievable through following a strategy and the sum of the normalised stand deviations represents a measure of the precision. The objective function is therefore defined as

$$\text{Objective function} = w_1 \times \left(\sum \hat{\mu}_e \right) + w_2 \times \left(\sum \hat{\sigma} \right),$$

where $\hat{\mu}_e$ is the normalised mean error, $\hat{\sigma}$ is the normalised standard deviation, w_1 and w_2 are weights and $w_1 + w_2 = 1$.

The search space is explored by creating a grid of template strategies for each number of manoeuvres (e.g. two glide slope and one slow down manoeuvre). These templates are then used to create n strategies by randomly populating the template with non-repeating manoeuvres from the manoeuvre pool. Each strategy is evaluated using the Monte Carlo process and the objective function.

This process relies on real flight data, which is subject to random (as well as systematic) errors. As a result, each individual manoeuvre may perform slightly better or worse than anticipated. A gust may cause a glide to sweep through a larger range of angles of attack than expected, or may upset a slow down through rapid changes in airspeed. Hence, the optima found through the heuristic described above may not be robust, that is, they may perform very well in a specific set of conditions, but they may not generalise well across a range of conditions. Thus we need to find robust strategies that maximise the accuracy of the estimates of aerodynamic coefficients within a given time budget.

We achieve this by taking the previously calculated strategies for each number of manoeuvres and evaluating the strategies for their dependence on individual manoeuvres (robustness). We created new sub-strategies by first replacing each glide slope manoeuvre with a new glide slope manoeuvre in the same airspeed range. This is done twice to double the number of sub-strategies – for a strategy with two glides, this would result in four sub-strategies. Each sub-strategy is then evaluated three further times with the slow down manoeuvres replaced with random slow down manoeuvres. An example of this process using an arbitrary four manoeuvre strategy is shown in Fig. 26 where first the glide slope manoeuvres are replaced to generate the initial sub-strategies and then the slow down manoeuvres are replaced for each glide slope configuration. This example would result in 12 sub-strategies. The resulting sub-strategies' objective functions (as determined through the Monte Carlo process) can then be averaged to get a robust estimate of the objective function of the strategy.

The resulting optimal strategies are presented in Figs 27 and 28 for the low windspeed and high windspeed sets respectively. The glide slope manoeuvres are represented by the appropriate gliding airspeed and the slow down manoeuvres are represented by *SDx* where *x* is an identification number. Pareto fronts are a useful tool for displaying the results of multi-objective optimisation, in this case, minimising the number of manoeuvres and minimising the robust objective function. Going from left to right, the first point is the absolute minimum for the number of manoeuvres and the optimum robust objective
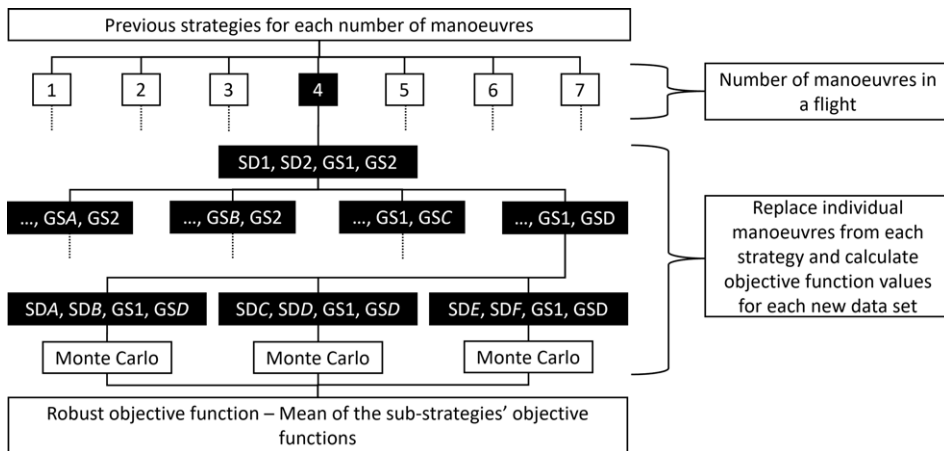
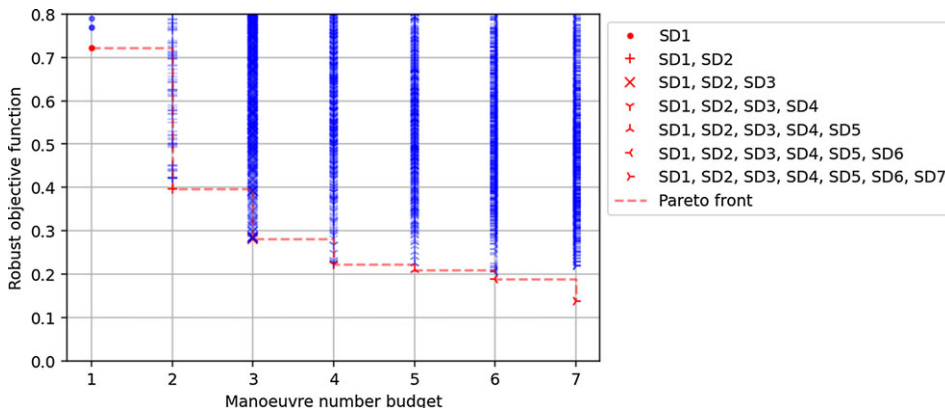**Figure 26.** *Robust optimisation process visualisation.*

Figure 27. *Pareto front for optimal strategy determination – low windspeed data.*
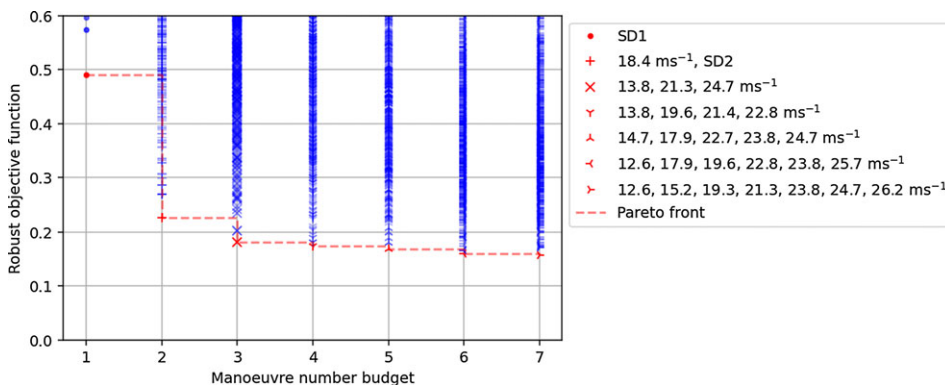

Figure 28. *Pareto front for optimal strategy determination – high windspeed data.*

function value for this. Each subsequent point increases the number of manoeuvres but decreases the robust objective function value. Hence, the Pareto front presents a series of optimal objective function combinations.

The figures demonstrate that each windspeed condition has a different optimal strategy set associated with it. The low windspeed condition (Fig. 27) yields slow down only strategies. The high windspeed condition (Fig. 28), in contrast, starts with a slow down (by necessity, as a single manoeuvre strategy can only be one that sweeps the entire alpha range), followed by a mixed two-manoeuvre strategy, and then switches to glide slope only strategies. Note also how the robust optimisation yields strategies that vary the gliding airspeed; this is expected, as it then facilitates the uniform coverage of the indicated airspeed range (recall that FliTePlat's minimum and maximum safe gliding airspeeds are 12 and 27m/s, respectively).

From this, it is clear that in windy conditions the accuracy of the glide slope manoeuvre is more robust, but in calm conditions superior accuracy is observed when flying slow down manoeuvres. This is because, while it is more efficient at covering the required range of angles of attack, the slow down manoeuvre is more susceptible to disturbances.

So how well are these results likely to generalise across the aircraft scale spectrum? While the manoeuvres themselves are scale-agnostic, the experiments we conducted here focused on the case of small aircraft limited to a 500m operating radius (within visual line of sight) and planetary boundary layer operations (below 400ft). This means that the results are only applicable to low altitude and limited area operations, which are characterised by ground-atmosphere interactions (turbulence) and by limited availability to straight ground track segments and glide descent lengths.

5.0 Conclusion

In this paper we considered various ways of obtaining lift and drag curves for a low cost, battery powered fixed wing platform. We examined the challenges and advantages associated with each method, and we conducted wind tunnel testing to serve as a repeatable (though subject to its own errors) reference.

The flight test methods consistently show a lower $C_{L\alpha}$ compared to the wind tunnel-derived values, indicating that the ideal test environment of the wind tunnel presents significant limitations in terms of its representativeness of real world operations. As for the drag curve plots, the power-on methods show a lower C_{D0} compared to the unpowered methods due to the drag from the stationary propellers affecting the latter.

Due to the automated glide slope and slow down methods requiring the same equipment setups, the methods can be used interchangeably. We presented a Monte-Carlo heuristic that allows us to derive strategies for their optimal mixing, given a budget of manoeuvres available per flight, and given a mean windspeed. The results generated via our proposed robust design heuristic show that the slow down manoeuvre benefits from lower windspeeds whereas the glide slope manoeuvre results in higher accuracy data at higher windspeeds.

The analysis presented here, particularly the framework created for establishing time-optimal manoeuvre schedules, can be extended to other system identification tasks, both in terms of the performance of uncrewed platforms, as well as their handling qualities. Such comprehensive flight testing methodologies, designed around the specific requirements of light drones, will be increasingly important with the proliferation of a wide variety of platforms comprising the uncrewed air systems of the future, many featuring layouts with very limited legacy data. Of particular importance, in terms of extending the methodology described here, will be flight test campaigns designed to establish contingency handling qualities, with a particular focus on drones' control systems' ability to recover from upsets caused by propulsion system failures and other contingency scenarios.

Competing interests. The authors declare that they have no known competing financial interests or personal relationships that could have appeared to influence the work reported in this paper.

References

[1] Boyd, C., Westcott, O., Ferraro, M., Erbil, M.A. and Entwistle, R., CASCADE Open Aircraft Project: University of Southampton VTOL Drone Development, *AIAA Scitech* 2021 *Forum*, American Institute of Aeronautics and Astronautics, Reston, Virginia, 2021, pp 1–35.

[2] Ostler, J.N., Bowman, W.J., Snyder, D.O. and McLain, T.W. Performance flight testing of small, electric powered unmanned aerial vehicles, *Int. J. Micro Air Veh.*, 2009, **1**, (3), pp 155–171.

[3] Bergmann, D.P., Denzel, J., Pfeifle, O., Notter, S., Fichter, W. and Strohmayer, A. In-flight lift and drag estimation of an unmanned propeller-driven aircraft, *Aerospace*, 2021, **8**, (43), pp 1–16.

[4] Pfeifle, O., Notter, S., Fichter, W., Bergmann, D.P., Denzel, J. and Strohmayer, A. Verifying the effect of wingtip propellers on drag through in-flight measurements, *J. Aircr.*, 2022, **59**, (2), pp 474–483.

[5] Bronz, M., Garcia de Marina, H. and Hattenberger, G. In-flight thrust measurement using on-board force sensor, *AIAA Atmospheric Flight Mechanics Conference*, American Institute of Aeronautics and Astronautics, Reston, Virginia, 2017, pp 1–11.

[6] Gong, A., Maunder, H. and Verstraete, D., Development of an in-flight thrust measurement system for UAVs, *53rd AIAA/SAE/ASEE Joint Propulsion Conference,* 2017, 53, (July).

[7] McCrink, M.H. and Gregory, J.W. Design and development of a high-speed UAS for beyond visual line-of-sight operations, *J. Intell. Robot. Syst. Theory Appl.*, 2021, **101**, (2), pp 1–16.

[8] Srivastava, A., Kumar, A. and Ghosh, A.K. Determination of parameters during quasi-steady stall maneuver using genetic algorithm, *Int. J. Aviat. Aeronaut. Aerosp.*, 2019, **6**, (4), pp 1–23.

[9] Dantsker, O.D., Yu, S., Vahora, M. and Caccamo, M. Flight testing automation to parameterize unmanned aircraft dynamics, *AIAA Aviation 2019 Forum*, American Institute of Aeronautics and Astronautics, Reston, Virginia, 2019, pp 1-47.

[10] Tomaszewski, A. and Goraj, Z.J. Assessment of a small UAV speed polar graph by conducting flight tests, *Aircr. Eng. Aerosp. Technol.*, 2018, **91**, (5), pp 720–727.

[11] Cotting, M.C., Wolek, A., Murtha, J.F. and Woolsey, C.A. Developmental flight testing of the spAARO UAV, *48th AIAA Aerospace Sciences Meeting Including the New Horizons Forum and Aerospace Exposition*, Orlando, Florida, USA, 2010, pp 3439–3454.

[12] MakeFlyEasy, MakeFlyEasy, 2020. http://www.makeflyeasy.com/. Accessed on: 03 December 2020.

[13] Weishäupl, A., Scanlan, J. and Sobester, A. Flight test driven development of low cost UAVs – Pitfalls and opportunities, *AIAA Scitech 2023 Forum*, AIAA, Washington, DC, USA, 2023, p 14.

[14] University of Southampton, The R. J. Mitchell Wind Tunnel, 2022. https://www.southampton.ac.uk/research/facilities/large-wind-tunnel-3.5m-by-2.4m-by-10.5m. Accessed on: 15 February 2022.

[15] Marques, P. and Da Ronch, A. *Advanced UAV Aerodynamics, Flight Stability, and Control: Novel Concepts, Theory and Applications*, Wiley, Chichester, UK, 2017.

[16] Sobron, A., LuNdström, D. and Krus, P. A review of current research in subscale flight testing and analysis of its main practical challenges, *Aerospace*, 2021, **8**, (3), p 74.

[17] Nepomuceno, L.M., da Silva, R.G.A., Sobron, A., Krus, P. and LunDstrom, D. Estimation of lift characteristics of a subscale fighter using low-cost experimental methods, *Aircr. Eng. Aerosp. Technol.*, 2022, **94**, (March), pp 1379–1389.

[18] Traub, L.W. Range and endurance estimates for battery-powered aircraft, *J. Aircr.*, 2011, **48**, (2), pp 703–707.

[19] Zhang, R., Xia, B., Li, B., Cao, L., Lai, Y., Zheng, W., Wang, H., Wang, W. and Wang, M. A study on the open circuit voltage and state of charge characterization of high capacity lithium-ion battery under different temperature, *Energies*, 2018, **11**, (9), p 2408.

[20] Weishäupl, A. AutoFLpy documentation, 2020. https://autoflpy.readthedocs.io/en/latest/readme.html. Accessed on: 27 February 2020.

[21] Lemke, J.U., Kammerer, G.E. and Murashige, R.H. Aircraft propeller thrust measurement apparatus, US Patent Number US005524494A, 1996.

[22] McArthur, J.M. Strain gauge and accelerometer measurement for thrust estimation, European Patent Number EP15163075A1, 2015.

[23] Mettler, B.F. Extracting micro air vehicles aerodynamic forces and coefficients in free flight using visual motion tracking techniques, *Exp. Fluids*, 2010, **49**, (3), pp 557–569.

[24] Uhlig, D. and Selig, M. Stability characteristics of micro air vehicles from experimental measurements, *29th AIAA Applied Aerodynamics Conference*, 29, American Institute of Aeronautics and Astronautics, Reston, Virigina, 2011, pp 1–13.

[25] Laminar Research, X-Plane 11, 2020. https://www.x-plane.com/. Accessed on: 04 May 2020.

[26] Laminar Research, PlaneMaker, 2020. https://developer.x-plane.com/manuals/planemaker/. Accessed on: 04 May 2020.

[27] Laminar Research, X-Plane Blade Element Theory, 2020. https://www.x-plane.com/desktop/how-x-plane-works/. Accessed on: 08 April 2020.

[28] Boker, U., Henzinger, T.A. and Radhakrishna, A. Battery transition systems, *Proceedings of the 41st ACM SIGPLAN-SIGACT Symposium on Principles of Programming Languages – POPL '14*, 49, 2014, pp 595–606.

[29] Gudmundsson, S. Thrust modeling for propeller, *General Aviation Aircraft De-sign: Applied Methods and Procedures*, Butterworth-Heinemann, Oxford, UK, 2022.

[30] Giljarhus, K. pyBEMT: An implementation of the blade element momentum theory in Python, *J. Open Source Softw.*, 2020, **5**, (53), p 2480.

[31] APC Propellers. APC propellers, 2022. https://www.apcprop.com/technical-information/performance-data/. Accessed on: 30 May 2022.

[32] Voskuijl, M., van Bogaert, J. and Rao, A.G. Analysis and design of hybrid electric regional turboprop aircraft, *CEAS Aeronaut. J.*, 2018, **9**, (1), pp 15–25.

[33] Hastie, T., Tibshirani, R. and Friedman, J. *The Elements of Statistical Learning*, Springer New York, New York, New York, 2009.